



# The composition of the incipient partial melt of garnet peridotite at 3 GPa and the origin of OIB

F.A. Davis <sup>a,\*</sup>, M.M. Hirschmann <sup>a</sup>, M. Humayun <sup>b,1</sup>

<sup>a</sup> Department of Geology and Geophysics, 108 Pillsbury Hall, University of Minnesota, Minneapolis, MN 55455, USA

<sup>b</sup> Department of Earth, Ocean, & Atmospheric Science, and National High Magnetic Field Laboratory, Florida State University, Tallahassee, FL 32310-4100, USA

## ARTICLE INFO

### Article history:

Received 12 February 2011

Received in revised form 6 June 2011

Accepted 7 June 2011

Available online 6 July 2011

Editor: R.W. Carlson

### Keywords:

experimental petrology

ocean island basalt

partial melting

garnet peridotite

## ABSTRACT

We determined experimentally the composition of an incipient partial melt of a garnet lherzolite similar to KLB-1 peridotite at 3 GPa using modified iterative sandwich experiments (MISE). The MISE method enables microbeam analyses of quenched liquids that are in equilibrium at the onset of melting (nominally, 0% melt fraction) with a specified peridotite bulk composition. The equilibrium incipient partial melt is a TiO<sub>2</sub>-enriched (2.5 ± 0.2 wt.%) alkali olivine basalt with 44.8 ± 0.2 wt.% SiO<sub>2</sub> and 15.8 ± 0.1 wt.% MgO. Therefore, it has some compositional characteristics similar to a plausible parent to many alkalic oceanic island basalts. But in detail, several key components of this melt are different from parental liquids of typical primitive alkalic OIB, including lower FeO\* (9.7 ± 0.1 wt.%) and higher Al<sub>2</sub>O<sub>3</sub> (12.7 ± 0.2 wt.%). It is also distinct from basalts derived from the EM and HIMU mantle end-members. We conclude that the vast majority of alkalic OIB cannot originate from volatile-poor partial melting of garnet peridotite at the base of the oceanic lithosphere unless there are contributions from non-peridotitic lithologies and/or enrichment in volatiles, iron, or other metasomatic components, and that such lithologic heterogeneities are intrinsic features of the HIMU and EM mantle reservoirs.

© 2011 Elsevier B.V. All rights reserved.

## 1. Introduction

The compositions of oceanic island basalts (OIB) provide crucial information about Earth's interior, constraining the history of exchange between the mantle and the surface (Hofmann, 1997) and the thermal vigor of convective upwellings (Herzberg et al., 2007; Putirka, 2008). Unraveling the petrologic character of OIB sources has considerable bearing on both of these, but there is no consensus on the lithologies or the temperatures of OIB sources (Dasgupta et al., 2010; Herzberg, 2006). It is well established from radiogenic isotope ratios that mantle-derived basalts sample several distinct chemical reservoirs (Zindler and Hart, 1986), but the source lithologies responsible for the major element compositions spanned by OIB are not well constrained. Jackson and Dasgupta (2008) demonstrated that isotopic signatures in OIB lavas correlate with olivine fractionation-corrected major element compositions, in particular <sup>206</sup>Pb/<sup>204</sup>Pb with CaO/Al<sub>2</sub>O<sub>3</sub>, SiO<sub>2</sub>, and FeO\* and <sup>87</sup>Sr/<sup>86</sup>Sr with K<sub>2</sub>O. They were able to resolve the mantle end-members, EM1, EM2, and HIMU (Zindler and Hart, 1986) from concentrations of major and minor elements, suggesting that each represents not only a reservoir that experienced a particular isotopic fractionation event, but also is associated with a particular melting lithology, volatile enrichment, and/or set of

pressure–temperature conditions. It is through partial melting experiments at temperatures and pressures conducive to melting in the mantle, and with potential melting sources like peridotites and pyroxenites that these chemical trends will be linked to their sources.

Experimentally-produced compositions of partial melts of garnet peridotite (Hirose and Kushiro, 1993; Walter, 1998) have not resembled key features of alkalic OIB, including TiO<sub>2</sub>, CaO, FeO\*, and Al<sub>2</sub>O<sub>3</sub> concentrations (Hirschmann et al., 2003). These compositional characteristics may require enrichments in CO<sub>2</sub> (Dasgupta et al., 2007a), or participation of recycled crustal or metasomatic lithologies (Kogiso et al., 1998; Kogiso et al., 2003; Pilet et al., 2005). Establishment of links between volatile-enrichments and/or recycled crustal components in OIB, and in particular in HIMU or EM sources, is of the highest importance for documenting the dynamics of mantle convection and the operation of deep Earth volatile cycles, but the role of these exotic components cannot be evaluated without accurate constraints on compositions of small-degree melts from volatile-free garnet peridotite.

Experimental determinations of compositions of small-degree partial melts of peridotite are elusive because melts in close proximity to crystals are modified by crystallization during quench (Mysen and Kushiro, 1977). Low melt fraction (*F*) liquids of spinel-facies peridotite have been documented at pressures <2 GPa by segregating melt from crystals in melt traps (Baker et al., 1995; Hirose and Kushiro, 1993; Pickering-Witter and Johnston, 2000; Wasylenki et al., 2003) and by sandwich techniques (Robinson et al., 1998), but compositions of small-degree partial melts of garnet lherzolite have

\* Corresponding author. Tel.: +1 612 625 0366; fax: +1 612 625 3819.

E-mail addresses: [davis957@umn.edu](mailto:davis957@umn.edu) (F.A. Davis), [mmh@umn.edu](mailto:mmh@umn.edu)

(M.M. Hirschmann), [humayun@magnet.fsu.edu](mailto:humayun@magnet.fsu.edu) (M. Humayun).

<sup>1</sup> Tel.: +1 850 644 1908; fax: +1 850 644 0827.

not been determined. Yet, it is just such compositions, formed at conditions present beneath mature oceanic lithosphere, which are needed to understand the origin of alkalic OIB. Experiments documenting the compositions of partial melts of garnet lherzolite from 3 to 7 GPa have been limited to higher melt fractions (>5%, Hirose and Kushiro, 1993; Walter, 1998), and virtually all yielded tholeiitic rather than alkalic liquids. Further, whereas strong signatures of residual garnet are common in both alkalic OIB (McKenzie and O'Nions, 1995; Thomas et al., 1999; Yang et al., 2003) and continental intraplate alkali basalts (Baker et al., 1997; Class et al., 1994; Cook et al., 2005), all partial melting experiments in the garnet peridotite facies below 4 GPa exhausted garnet from the residue (Hirose and Kushiro, 1993; Walter, 1998). Thus, they do not constrain the petrologic character of partial melts potentially analogous to the parental liquids of alkalic OIB. The effects of pressure and composition on garnet peridotite partial melts have been explored in multiple saturation experiments (Longhi, 2002), but these are not easily relatable to a particular melt fraction or upper mantle lithology.

Using iterative partial melting experiments, we have determined the composition of the incipient partial melt (0% melting) at 3 GPa of a synthetic oxide mixture similar to KLB-1 peridotite (KLB-1ox, Table 1; Davis et al., 2009; Herzberg et al., 1990; Takahashi, 1986). This major element composition is thought to resemble the primitive mantle (McDonough and Sun, 1995) and the convecting upper mantle sampled by mid-ocean ridge basalts (Salters and Stracke, 2004; Workman and Hart, 2005). We are able to produce partial melts at a 0% melt fraction using the modified iterative sandwich experiment method (MISE; Hirschmann and Dasgupta, 2007), by which we force a basaltic melt into equilibrium with the solidus mineral assemblage through an iterative series of experiments. This composition allows evaluation of the role of normal garnet peridotite with low volatile content in the petrogenesis of alkalic OIB.

## 2. Experimental and analytical methods

### 2.1. MISE method

The incipient partial melt of a particular peridotite at a given pressure is the melt that is in equilibrium with the assemblage and compositions of minerals found in that lithology at the solidus temperature. The MISE method (Hirschmann and Dasgupta, 2007) works by equilibrating a putative melt composition with the residual

minerals of the peridotite at the solidus temperature. The resulting melt and mineral compositions are then used to determine mineral/melt partition coefficients ( $D_i^{min/melt}$ ) for each oxide ( $i$ ). Given a set of partition coefficients for each oxide in each mineral, the composition of the starting peridotite, and the mineral mode of the peridotite below the solidus (Table 1), a new putative melt composition can be estimated, which is synthesized for use as the starting melt in the next experimental step. In each subsequent experiment, a new putative melt composition is added to the original peridotite until the resulting melt and mineral compositions cease to change. This final melt composition is in equilibrium with the solidus minerals and therefore is equivalent to a partial melt of the peridotite with a melt fraction of 0%. (See Hirschmann and Dasgupta, 2007 for a complete explanation of the MISE method).

### 2.2. Piston cylinder experiments

#### 2.2.1. Experimental setup

Experiments were conducted with peridotitic and basaltic synthetic oxide mixtures (see Appendix for method of starting material synthesis) at 3 GPa in a 1/2" piston cylinder apparatus at the University of Minnesota using the experimental assemblies, procedures, and calibrations described by Xirouchakis et al. (2001). Starting materials were packed into a graphite inner capsule and then sealed in a platinum outer capsule with an external diameter of ~4 mm. All experiments were run for 24 h, which was considered sufficient to approach equilibrium. Note that successful application of the MISE method does not require that each experimental iteration achieve equilibrium, so long as equilibrium is approached in each step (Hirschmann and Dasgupta, 2007).

#### 2.2.2. The solidus of KLB-1ox

To locate the solidus of KLB-1ox at 3 GPa, we performed 24-hour experiments using only the KLB-1ox mixture near the presumed dry peridotite solidus (Hirschmann, 2000) at temperatures of 1430, 1440, 1450, and 1460 °C. These capsules were examined for signs of melt at high magnification using the JEOL 6500 field-emission gun scanning electron microscope (FEG-SEM) at the Characterization Facility of the University of Minnesota. In experiments at 1450 and 1460 °C, small (~0.5 μm) triangular melt pockets in grain boundary triple junctions are common, indicating production of very small fractions of melt (Fig. 1). Triple junctions are always melt-free in experiments at 1430 and 1440 °C indicating subsolidus conditions. These experiments appear to bracket the solidus to within ± 5 °C, but given inevitable uncertainties in temperature reproducibility of piston cylinder experiments, we conclude that the solidus likely resides within ± 15° of 1445 °C.

Once the solidus temperature had been established, we conducted a longer, 168-hour, experiment at 1430 °C to determine the compositions and modes of near-solidus minerals of KLB-1ox. The mineral mode (Table 1) was determined by mass balance (Table 2).

#### 2.2.3. MISE experiments

Five MISE iterations were performed near the solidus of KLB-1ox. At each step a starting mix was made by combining 20% (by weight) of the putative melt composition (Supplementary Table 1) and 80% KLB-1ox. The mix was homogenized by grinding with an agate mortar and pestle under ethanol for 1–2 h. Ideally, individual experiments produce large melt pools at a melt fraction of 20%. Owing to minor variations in experimental temperatures, weighing errors during synthesis, and a significant change to the amount of K<sub>2</sub>O added to the melt phase after the first two iterations (see Appendix), individual experiments showed variation in their experimental melt fractions. To ensure that several charges at each iteration had experimental melt fractions near 20%, 3–5 experiments were run at a range of temperatures from 1450 to 1470 °C during each iteration step.

**Table 1**

Composition of the starting peridotite, final 0% melt determination, and estimates of mantle compositions.

	KLB-1ox <sup>a</sup>	err	0% melt	err	PUM <sup>b</sup>	DMM <sup>c</sup>
SiO <sub>2</sub>	44.92	0.22	44.77	0.15	45.0	44.71
TiO <sub>2</sub>	0.16	0.02	2.45	0.19	0.201	0.13
Al <sub>2</sub> O <sub>3</sub>	3.92	0.07	12.70	0.16	4.45	3.98
Cr <sub>2</sub> O <sub>3</sub>	0.28	0.02	0.12	0.01	0.384	0.57
FeO*	8.09	0.15	9.72	0.09	8.05	8.18
MnO	0.12	0.03	0.14	0.02	0.135	0.13
MgO	38.76	0.26	15.78	0.07	37.8	38.73
CaO	3.79	0.06	10.80	0.19	3.55	3.17
Na <sub>2</sub> O	0.30	0.04	2.52	0.16	0.36	0.28
K <sub>2</sub> O	0.014	0.002	0.99 <sup>d</sup>	0.30	0.029	0.006
Total	100.354		100.00		99.959	99.886
<i>Subsolidus mode at 3 GPa</i>						
Olivine	60.8					
opx	7.7					
cpx	22.6					
Garnet	8.9					

<sup>a</sup> Following method of Davis et al. (2009).

<sup>b</sup> McDonough and Sun (1995).

<sup>c</sup> Workman and Hart (2005).

<sup>d</sup> For a peridotite with K<sub>2</sub>O = 0.003±0.001% wt. (see Supplement).

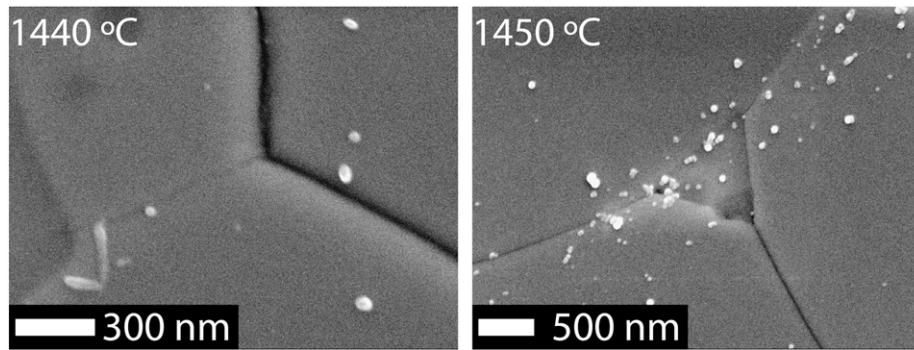


**Fig. 1.** Field-emission gun scanning electron microscope (FEG-SEM) secondary electron images of solidus location experiments. At 1440 °C (left), mineral grains meet at triple junctions lacking evidence of melt, but at 1450 °C (right), many triple junctions are filled with triangular patches (~0.5 μm) of quenched melt, indicating the onset of partial melting. White particles on top of sample are the remnants of colloidal silica polishing compound.

## 2.3. Analytical techniques

### 2.3.1. Electron microprobe analysis (EMP)

Capsules were mounted on brass plugs in epoxy and polished with successively finer loose diamond powders on nylon pads to a finish of 1 or 0.25 μm, and a thin (5–20 nm) conductive carbon coat was applied to polished sections. Major element analysis and imaging of the MISE experiments were performed using the JEOL JXA-8900 electron microprobe at the University of Minnesota.

Quantitative analysis of the run products was performed with an accelerating voltage of 15 kV, and a focused spot (<1 μm diameter). Count times for all oxides, except K<sub>2</sub>O analyses of minerals (see next paragraph) and Na<sub>2</sub>O, were 10 s off-peak and 20 s on-peak. To minimize Na<sub>2</sub>O migration, Na<sub>2</sub>O count times were 5 s off peak and 10 s on, and Na<sub>2</sub>O was analyzed on the first pass of the spectrometers. The beam current was 10 nA for quenched melt and 15 nA for mineral phases. Mineral grains were typically 10–50 μm in diameter. 20 microprobe points, each on different grains located in different parts of the capsule, were collected for each mineral phase in each experiment. Analyses with totals >101% or <99% were discarded as were analyses giving poor stoichiometry ( $\pm 0.01$  total cations) calculated on a 4- (olivine), 6- (pyroxenes), or 12- (garnet) oxygen basis, and reported compositions are averages of the remaining analyses (5–20 analyses per reported phase). There was little variation between individual spots, suggesting that the mineral phases were homogeneous and approached equilibrium during the experiment.

A separate technique was used to measure K<sub>2</sub>O in the minerals, owing to very low concentrations. These were performed with an accelerating voltage of 15 kV and a 5 μm defocused beam with a beam current of 200 nA. Count times were 50 s on peak and 50 s off peak. Points were taken from twenty different grains of each mineral phase,

**Table 2**  
Subsolidus mineral compositions.

	Olivine	s.d.	opx	s.d.	cpx	s.d.	Garnet	s.d.
n	16		16		16		11	
SiO <sub>2</sub>	40.65	0.16	54.28	0.24	52.97	0.41	42.15	0.35
TiO <sub>2</sub>	0.01	0.03	0.22	0.03	0.33	0.04	0.50	0.07
Al <sub>2</sub> O <sub>3</sub>	0.15	0.04	5.22	0.24	5.90	0.41	22.76	0.43
Cr <sub>2</sub> O <sub>3</sub>	0.06	0.03	0.47	0.04	0.58	0.05	1.16	0.11
FeO*	10.00	0.12	5.89	0.10	4.82	0.18	6.63	0.13
MnO	0.14	0.02	0.11	0.02	0.12	0.02	0.20	0.02
MgO	48.26	0.30	31.16	0.34	21.43	0.78	20.50	0.26
CaO	0.27	0.08	2.31	0.48	12.64	0.81	5.80	0.41
Na <sub>2</sub> O	0.03	0.02	0.22	0.04	1.01	0.04	0.04	0.03
K <sub>2</sub> O	0.009	0.012	n.d.		0.009	0.011	n.d.	
Total	99.579		99.88		99.809		99.74	

s.d. = standard deviation.  
n.d. = not detected.

and obvious outliers were removed from the average (higher concentrations presumably came from overlap with melt filled grain interstices). This method was used to determine K<sub>2</sub>O concentrations of minerals in iteration steps 3–5. For the subsolidus run and iteration steps 1 and 2, K<sub>2</sub>O was analyzed following the procedure described above for other oxides. Analyses of secondary standards with low K<sub>2</sub>O concentrations are provided in Supplementary Table 2 to demonstrate the precision of low-concentration K<sub>2</sub>O analyses by EMP.

The heterogeneous character of the quenched melt in the experimental charges required collection of many analytical spots (>100) to determine an accurate mean composition. Spots were chosen by analyzing at 2–3 μm intervals along linear traverses. Spots chosen in this way avoid collection of a biased set of data, as may result from manual spot selection. The simple average of spots collected in this way does not always give the correct composition of the equilibrium melt phase because certain fragile quench components are unavoidably lost during polishing, skewing the average toward more physically robust quench products (Fig. 2). To determine the points that give a representative average, a filtering procedure was applied excluding individual analyses judged to have compositions outside the expected range of Fe–Mg exchange equilibrium between olivine and melt ( $K_D^{Fe-Mg} = [X_{Fe}^{ol} X_{Mg}^{liq}] / [X_{Mg}^{ol} X_{Fe}^{liq}]$ ). Analyses of quenched liquid were normalized to 100%, and  $K_D^{Fe-Mg}$  was calculated

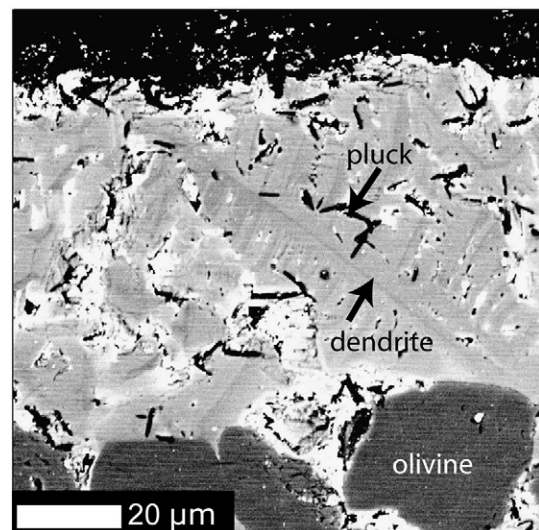


**Fig. 2.** Back-scattered electron (BSE) image of quenched melt region. From A682 (iteration step 3), the light gray region is a matte of quench products displaying the dendritic habit of quench crystals. Small black slivers are holes left by fragile quench products unavoidably lost during polishing. Dark gray at the bottom of the image are olivine crystals, and the black at the top is the edge of the inner graphite liner.

for each point using the average composition of coexisting olivine. A model  $K_D^{Fe-Mg}$  was also determined for each analyzed melt composition following the method of Toplis (2005), and all points with differences between measured and modeled  $K_D^{Fe-Mg}$  greater than the model error ( $\pm 0.03$ ) were discarded. The remaining points were averaged to yield an estimate of the equilibrium melt composition. The  $K_D^{Fe-Mg}$  filtering method does not identify parts of the melt pools that preserve equilibrium with coexisting olivine, but rather provides a method for isolating a set of points that most closely represent the average composition of the melt. This reduces the possibility of the average of analytical spots being strongly influenced by the absence of a particular component of the quench which is easily lost during polishing (Fig. 2). Additional processing was required to determine CaO and K<sub>2</sub>O contents of the melts; a discussion of this method can be found in the Appendix.

### 2.3.2. Laser ablation inductively-coupled plasma mass spectrometry (LA-ICP-MS)

To check the accuracy of melt compositions determined by EMP and  $K_D^{Fe-Mg}$  filtering, several samples were analyzed by laser ablation inductively-coupled plasma mass spectrometry (LA-ICP-MS) at Florida State University. Because LA-ICP-MS is a volume technique (the volume sampled by each EMP probe spot is  $\sim 1 \mu\text{m}^3$ , while the volume sampled by each LA-ICP-MS data point is  $\sim 800 \mu\text{m}^3$  for a 20  $\mu\text{m}$  spot to  $\sim 3200 \mu\text{m}^3$  for a 50  $\mu\text{m}$  spot; Humayun et al., 2010), it is less affected by small surface irregularities induced by imperfect polishing.

LA-ICP-MS measurements were performed with a New Wave UP193FX (193 nm) ArF excimer laser ablation system coupled to a Thermo Element XR sector-field ICP-MS at Florida State University. A 20  $\mu\text{m}$  laser spot was scanned across the melt region at a rate of 5  $\mu\text{m}/\text{s}$ , and the melt composition was derived from an average of the points taken along the traverse. It is possible for ablation pits in the melt pool to also sample phases existing deeper in the charge, not visible at the surface. Analysis of sample A682 (iteration 3), for example, gave some points with MgO as great as 41 wt.%, clearly sampling olivine and opx

(see Humayun et al. (2010) for a more thorough discussion). To correct for this, analyses with MgO > 17 wt.% were discarded prior to averaging.

### 2.4. Determining convergence to the 0% melt

#### 2.4.1. Calculating the projected melt composition

After processing mineral and melt analyses, a new liquid composition must be projected for use as the starting melt in the subsequent MISE iteration. First, mineral/melt partition coefficients ( $D_i^{\text{min}/\text{melt}}$ ) were determined for each oxide ( $i$ ) in each mineral by dividing the concentration of that oxide in the mineral by its concentration in the melt ( $C_i^{\text{min}}/C_i^{\text{melt}}$ ). The bulk partition coefficient ( $D_i^{\text{perid}/\text{melt}}$ ) can then be determined by summing the products of the mineral partition coefficients and the subsolidus mode as determined in Section 2.2.2 (Table 1). Dividing the composition of the peridotite oxide mix by the bulk partition coefficients give the composition of the projected 0% melt, which was then synthesized for the next iteration.

#### 2.4.2. Monitoring convergence to the 0% partial melt composition

After a sufficient number of iterations, the melt present at the end of an experiment should be the same as the melt composition calculated from the previous experiment. This melt composition represents the 0% partial melt of the peridotite. Three criteria were monitored to determine convergence to this ideal composition:

1. Convergence of measured and projected melt compositions within each iteration step
2. Stability of the projected melt composition, and therefore the bulk partition coefficients, over several iteration steps
3. Convergence of the residual mineral compositions with those of the subsolidus minerals

As the composition of the projected melt approaches the equilibrium composition, the composition of melt coexisting with peridotite after each experiment should also become more similar to

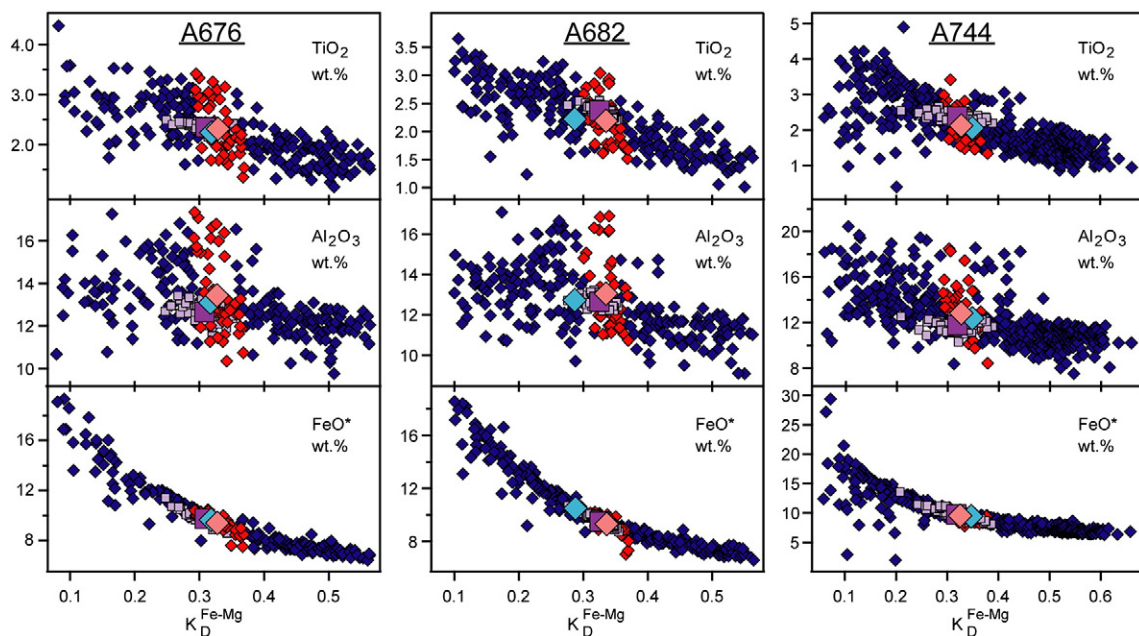


**Fig. 3.** Comparison of the EMP and LA-ICP-MS methods for analyzing the composition of the heterogeneous melt pools. The vertical axes show oxide concentrations in weight percent. The horizontal axes show  $K_D^{Fe-Mg}$  determined from the composition of individual analysis points and the average composition of coexisting olivine in the charge. Small blue diamonds are EMP analyses excluded from the average for not matching model  $K_D^{Fe-Mg}$  (Toplis, 2005). Small red diamonds are EMP analyses that passed the  $K_D^{Fe-Mg}$  filter and are included in the average. Small purple squares are LA-ICP-MS analyses. The large blue diamond shows the average composition determined by including all EMP analyses. The large red diamond shows the average composition determined by using only points passing the filter. The large purple square is the average of the LA-ICP-MS analyses.

the melt projected from the previous iteration. Fig. 4 shows this convergence by plotting the measured and projected compositions at each iteration step. For most components the difference between these compositions decreases with each successive iteration.

Small deviations in the observed melt compositions are expected owing to variations in experimental temperature, melt fraction, and uncertainty in the weighing steps, but we can be confident that the melt is near equilibrium if the partition coefficients do not vary between iterations. Because the projected melt composition depends only on the bulk partition coefficients, the stability of the partition coefficients for most components over the last three iterations (Fig. 4) suggests the ideal 0% melt was attained after the third iteration.

The minerals present in an experiment that has converged to the 0% melt composition should have the same composition as the minerals from the subsolidus experiment (Table 2). A comparison of mineral compositions is shown in Fig. 5. It is especially important to monitor incompatible elements, as their convergence is expected to require larger numbers of iterations (Hirschmann and Dasgupta, 2007). Clinopyroxene is the chief mineral reservoir for both  $\text{TiO}_2$  and  $\text{Na}_2\text{O}$ , and the concentrations of these oxides in the residual cpx approach those of the subsolidus cpx by the final experiment, suggesting near equilibration. The concentration of the incompatible major element  $\text{Al}_2\text{O}_3$  in cpx also approaches the subsolidus composition at the end of the experimental series. Olivine Mg# ( $X_{\text{Mg}}/(X_{\text{Mg}} + X_{\text{Fe}})$ , molar quantities), primarily an indicator of temperature and melt

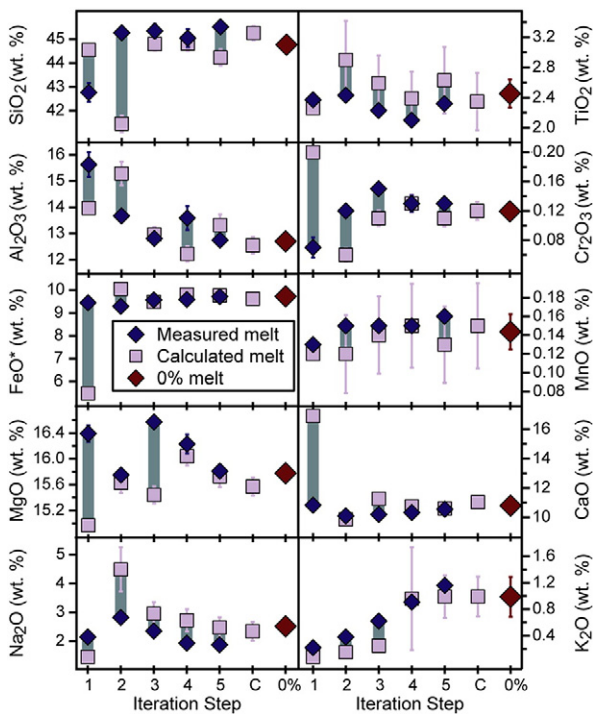


Fig. 4. Evolution of the melt layer through the successive experimental iterations. Blue diamonds are compositions, averaged within each iteration, of the melt phase existing in the capsules at the ends of the experimental runs. Error for individual experiments was calculated as the deviation of the mean (standard deviation/ $\sqrt{n}$ ); the error bars show these errors propagated through the average. Lavender squares are the compositions of the melt calculated by the MISE method (Hirschmann and Dasgupta, 2007) using the average measured mineral and melt compositions from the previous iteration (except iteration 1, where the “calculated” melt composition is the initial basalt composition). The melt composition calculated with partition coefficients determined from the final iteration step is denoted “C” on the horizontal axis. The red diamonds show the composition of the incipient melt of KLB-10x, calculated as the average of the predicted melts from experiments in the last three iterations and is denoted by “0%” on the horizontal axis (see Section 2.4.2).

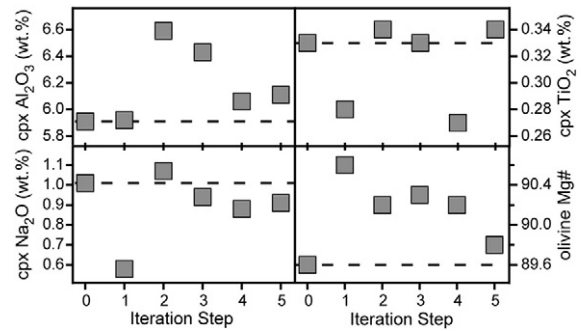


Fig. 5. Convergence of experimental mineral compositions to those of the subsolidus minerals. Each point is the average of cpx or olivine compositions from all experiments in a given iteration step. Step 0 corresponds to the subsolidus mineral composition. The dashed line is drawn through the subsolidus composition and is intended to highlight the ideal convergence point for the experimental mineral compositions.

fraction, also reaches similar values to the subsolidus minerals by the final step.

Theoretically, the composition of the 0% melt is that projected from the results of the final iteration. However, weighing errors and differences in experimental melt fraction owing to temperature variations contribute to small changes in melt composition for individual experiments. Therefore, even after the ideal melt composition has been approached, melt compositions change slightly in additional iterations. Consequently, we estimate the final 0% partial melt from an average of the projected melt compositions from the experiments performed in the last three iterations (Supplementary Table 3). To test whether differences in experimental melt fraction were affecting this average, the projected melt compositions from all experiments in the last three iteration steps were plotted against experimental melt fractions. A weighted least squares regression gives model compositions at  $F^{\text{exp}}=0.2$  (the ideal experimental melt fraction). For each oxide, the model and average compositions were the same within error (Supplementary Table 3). We report the composition determined by a simple average of the experiments in the last three iteration steps as the composition of the incipient partial melt of KLB-10x with  $\text{K}_2\text{O}=0.003 \pm 0.001$  wt.% (see appendix for the method of determining the model source  $\text{K}_2\text{O}$  content).

### 3. Results

The subsolidus mineral assemblage of KLB-10x determined at 3 GPa and 1430 °C consists of 60.8% olivine, 7.7% orthopyroxene, 22.6% clinopyroxene, and 8.9% garnet (Table 1). Clinopyroxene is subcalcic, with  $12.6 \pm 0.8$  wt.% CaO and clinopyroxene and orthopyroxene contain  $5.9 \pm 0.4$  and  $5.2 \pm 0.2$  wt.%  $\text{Al}_2\text{O}_3$ , respectively.

The average melt compositions obtained from filtered and unfiltered electron microprobe analyses are compared to those obtained by LA-ICP-MS for 3 experiments in Fig. 3 and Table 4. The LA-ICP-MS data compare favorably with both EMP averages for most components; however, the  $K_D^{\text{Fe}-\text{Mg}}$  of the filtered averages more consistently match both the LA-ICP-MS averages and, by definition, the  $K_D^{\text{Fe}-\text{Mg}}$  one would predict for a liquid in equilibrium with the coexisting olivines (Toplis, 2005). For this reason and because the filtered and unfiltered EMP averages differ in some cases, especially for incompatible elements like  $\text{TiO}_2$  and  $\text{Na}_2\text{O}$  (Table 4), the  $K_D^{\text{Fe}-\text{Mg}}$ -filtered EMP averages are preferred. The correspondence between the  $K_D^{\text{Fe}-\text{Mg}}$ -filtered EMP average and the LA-ICP-MS averages validates the  $K_D^{\text{Fe}-\text{Mg}}$  filtering method for determining the average composition of a heterogeneous quenched melt by electron microprobe analysis. We note that the compositions of partial melts, and most notably the  $\text{FeO}^*$  concentrations, determined by the method are model-dependent. However, independent verification of melt  $\text{FeO}^*$  concentrations by LA-ICP-MS indicates that these concentrations are not biased by the filtering method.

The 0% partial melt of volatile-free KLB-1ox at 3 GPa (Table 1) is an alkali olivine basalt (Schwarzer and Rogers, 1974) with  $44.8 \pm 0.2$  wt.%  $\text{SiO}_2$ ,  $15.8 \pm 0.1$  wt.% MgO, and  $3.5 \pm 0.3$  wt.% total alkalis ( $\text{Na}_2\text{O} + \text{K}_2\text{O}$ ). The melt is characterized by high CaO ( $10.8 \pm 0.2$  wt.%) and high CaO/ $\text{Al}_2\text{O}_3$  (0.85), and it is enriched in the incompatible elements  $\text{Na}_2\text{O}$  ( $2.5 \pm 0.2$  wt.%) and  $\text{TiO}_2$  ( $2.5 \pm 0.2$  wt.%).

## 4. Discussion

### 4.1. Comparison to previous experimental results at 3 GPa

The composition of the near-solidus partial melt of garnet peridotite at 3 GPa is compared to those determined from direct

**Table 3**  
Iteration average mineral and melt compositions.

	liq	err	ol	s.d.	opx	s.d.	cpx	s.d.	gt	s.d.
<i>Step 1</i>										
$\text{SiO}_2$	42.77	0.39	40.65	0.19	54.65	0.43	52.78	0.27	42.40	0.25
$\text{TiO}_2$	2.37	0.08	0.01	0.02	0.18	0.03	0.28	0.03	0.53	0.05
$\text{Al}_2\text{O}_3$	15.63	0.47	0.13	0.02	5.01	0.45	5.91	0.13	23.35	0.14
$\text{Cr}_2\text{O}_3$	0.07	0.01	0.10	0.03	0.42	0.02	0.53	0.03	1.13	0.13
$\text{FeO}^*$	9.44	0.11	9.02	0.10	5.21	0.12	4.19	0.14	5.75	0.09
MnO	0.13	0.01	0.11	0.03	0.11	0.02	0.12	0.03	0.19	0.03
MgO	16.39	0.13	49.02	0.21	32.04	0.25	21.58	0.34	21.24	0.31
CaO	10.83	0.18	0.24	0.02	2.23	0.09	13.77	0.43	5.77	0.34
$\text{Na}_2\text{O}$	2.15	0.12	0.01	0.02	0.12	0.02	0.58	0.03	0.01	0.01
$\text{K}_2\text{O}$	0.22	0.02	0.02	0.01	0.02	0.01	0.02	0.01	0.02	0.01
Total	100.00		99.31		99.99		99.76		100.39	
<i>Step 2</i>										
$\text{SiO}_2$	45.27	0.27	40.87	0.12	54.63	0.15	53.03	0.19	42.11	0.13
$\text{TiO}_2$	2.43	0.06	0.02	0.01	0.20	0.01	0.33	0.02	0.57	0.05
$\text{Al}_2\text{O}_3$	13.67	0.22	0.15	0.01	5.51	0.16	6.57	0.10	23.31	0.11
$\text{Cr}_2\text{O}_3$	0.12	0.01	0.08	0.01	0.45	0.02	0.56	0.02	1.06	0.03
$\text{FeO}^*$	9.29	0.08	9.51	0.04	5.62	0.05	4.69	0.08	6.29	0.06
MnO	0.15	0.01	0.12	0.02	0.11	0.01	0.12	0.01	0.19	0.01
MgO	15.75	0.10	48.96	0.17	31.45	0.14	21.92	0.25	21.00	0.13
CaO	10.10	0.11	0.23	0.01	2.13	0.03	11.42	0.27	5.17	0.13
$\text{Na}_2\text{O}$	2.83	0.07	0.03	0.01	0.27	0.02	1.06	0.03	0.03	0.01
$\text{K}_2\text{O}$	0.38	0.01	0.02	0.01	0.02	0.01	0.02	0.01	0.02	0.01
Total	100.00		99.99		100.39		99.72		99.75	
<i>Step 3</i>										
$\text{SiO}_2$	45.35	0.29	40.58	0.14	53.90	0.22	52.69	0.19	41.64	0.20
$\text{TiO}_2$	2.23	0.05	0.02	0.01	0.20	0.02	0.33	0.02	0.56	0.05
$\text{Al}_2\text{O}_3$	12.81	0.20	0.16	0.03	5.34	0.26	6.40	0.12	23.06	0.37
$\text{Cr}_2\text{O}_3$	0.15	0.01	0.09	0.01	0.45	0.02	0.56	0.02	1.09	0.05
$\text{FeO}^*$	9.57	0.10	9.38	0.08	5.53	0.06	4.60	0.10	6.25	0.05
MnO	0.15	0.01	0.11	0.01	0.11	0.02	0.11	0.01	0.17	0.01
MgO	16.57	0.10	49.20	0.20	31.52	0.13	21.96	0.25	20.88	0.18
CaO	10.20	0.12	0.23	0.01	2.22	0.04	12.03	0.29	5.36	0.14
$\text{Na}_2\text{O}$	2.36	0.07	0.04	0.02	0.23	0.02	0.93	0.03	0.03	0.01
$\text{K}_2\text{O}$	0.62	0.02	0.005	0.006	0.002	0.005	0.007	0.005	0.005	0.004
Total	100.00		99.815		99.502		99.617		99.045	
<i>Step 4</i>										
$\text{SiO}_2$	45.05	0.38	40.85	0.19	54.58	0.11	53.10	0.16	42.28	0.25
$\text{TiO}_2$	2.10	0.06	0.02	0.02	0.18	0.02	0.27	0.02	0.49	0.04
$\text{Al}_2\text{O}_3$	13.59	0.45	0.16	0.02	5.21	0.16	6.06	0.10	22.99	0.41
$\text{Cr}_2\text{O}_3$	0.13	0.01	0.08	0.01	0.48	0.02	0.58	0.03	1.26	0.03
$\text{FeO}^*$	9.59	0.10	9.50	0.08	5.57	0.06	4.59	0.08	6.20	0.06
MnO	0.15	0.01	0.12	0.01	0.12	0.02	0.13	0.02	0.20	0.02
MgO	16.23	0.15	49.16	0.18	31.75	0.12	21.97	0.32	21.03	0.18
CaO	10.32	0.17	0.23	0.02	2.21	0.04	12.41	0.34	5.45	0.17
$\text{Na}_2\text{O}$	1.94	0.07	0.02	0.01	0.20	0.02	0.88	0.04	0.03	0.02
$\text{K}_2\text{O}$	0.91	0.02	0.002	0.001	0.002	0.001	0.006	0.002	0.002	0.003
Total	100.00		100.142		100.302		99.996		99.932	
<i>Step 5</i>										
$\text{SiO}_2$	45.52	0.26	40.70	0.13	54.73	0.25	53.18	0.19	42.04	0.18
$\text{TiO}_2$	2.32	0.05	0.02	0.02	0.20	0.02	0.34	0.03	0.62	0.05
$\text{Al}_2\text{O}_3$	12.75	0.21	0.15	0.06	4.99	0.25	6.13	0.16	23.48	0.11
$\text{Cr}_2\text{O}_3$	0.13	0.01	0.08	0.02	0.44	0.02	0.56	0.03	1.03	0.06
$\text{FeO}^*$	9.71	0.08	9.86	0.08	5.72	0.07	4.75	0.10	6.53	0.06
MnO	0.16	0.00	0.12	0.02	0.12	0.02	0.13	0.02	0.20	0.02
MgO	15.81	0.10	48.87	0.19	31.62	0.13	21.91	0.41	20.69	0.15
CaO	10.55	0.12	0.24	0.05	2.21	0.05	12.30	0.46	5.45	0.18
$\text{Na}_2\text{O}$	1.88	0.04	0.02	0.01	0.22	0.02	0.92	0.03	0.03	0.01
$\text{K}_2\text{O}$	1.16	0.04	0.002	0.001	0.003	0.001	0.008	0.003	0.003	0.003
Total	100.00		100.062		100.253		100.228		100.073	

Liquid compositions reported are averages of normalized, filtered EMP analyses.

err = deviation of the mean (standard deviation/ $\sqrt{n}$ ).

s.d. = standard deviation.

**Table 4**

Melt layer average compositions for several experiments to compare the EMP and LA-ICP-MS methods.

	EMP (all)	err	EMP (filtered)	err	LA-ICP-MS	err
<b>A676</b>						
n	250		53		88	
SiO <sub>2</sub>	43.78	0.36	44.03	0.45	46.71	0.08
TiO <sub>2</sub>	2.08	0.03	2.23	0.07	2.34	0.01
Al <sub>2</sub> O <sub>3</sub>	12.34	0.11	13.03	0.23	12.68	0.04
Cr <sub>2</sub> O <sub>3</sub>	0.16	0.01	0.15	0.01	0.17	0.00
FeO*	9.02	0.13	9.14	0.10	9.80	0.05
MnO	0.15	0.00	0.14	0.01	0.17	0.00
MgO	15.33	0.21	15.58	0.13	15.72	0.06
CaO	8.98	0.12	9.01	0.20	9.22	0.03
Na <sub>2</sub> O	2.22	0.05	2.60	0.08	2.83	0.03
K <sub>2</sub> O	0.32	0.01	0.41	0.03	0.36	0.01
Total	94.38		96.32		100.00 <sup>a</sup>	
$K_D^{Fe-Mg}$	0.318	0.007	0.327	0.005	0.308	0.004
<b>A682</b>						
n	265		39		65	
SiO <sub>2</sub>	42.88	0.35	44.17	0.43	46.35	0.06
TiO <sub>2</sub>	2.07	0.03	2.13	0.07	2.35	0.01
Al <sub>2</sub> O <sub>3</sub>	11.88	0.11	12.70	0.30	12.60	0.03
Cr <sub>2</sub> O <sub>3</sub>	0.15	0.01	0.14	0.01	0.16	0.00
FeO*	9.83	0.16	9.12	0.13	9.41	0.04
MnO	0.15	0.00	0.14	0.00	0.16	0.00
MgO	15.24	0.22	16.11	0.16	16.54	0.04
CaO	9.03	0.13	9.57	0.27	9.64	0.04
Na <sub>2</sub> O	2.21	0.05	2.34	0.10	2.17	0.01
K <sub>2</sub> O	0.64	0.04	0.78	0.12	0.63	0.01
Total	94.08		97.20		100.00	
$K_D^{Fe-Mg}$	0.285	0.007	0.333	0.007	0.323	0.004
<b>A744</b>						
n	500		53		66	
SiO <sub>2</sub>	44.18	0.28	43.10	0.73	46.26	0.14
TiO <sub>2</sub>	1.92	0.04	2.00	0.06	2.37	0.01
Al <sub>2</sub> O <sub>3</sub>	11.56	0.08	12.00	0.25	11.71	0.06
Cr <sub>2</sub> O <sub>3</sub>	0.19	0.00	0.14	0.01	0.20	0.00
FeO*	9.02	0.13	9.14	0.18	9.91	0.12
MnO	0.16	0.00	0.16	0.01	0.18	0.00
MgO	15.65	0.19	14.85	0.25	15.61	0.09
CaO	9.86	0.13	9.74	0.35	10.15	0.08
Na <sub>2</sub> O	1.68	0.04	1.89	0.07	2.50	0.03
K <sub>2</sub> O	0.75	0.06	1.11	0.21	1.10	0.02
Total	94.97		94.13		100.00	
$K_D^{Fe-Mg}$	0.349	0.008	0.327	0.006	0.319	0.006

err = deviation of the mean (standard deviation/ $\sqrt{n}$ ).<sup>a</sup> Converting signal intensity ratios to weight % oxides involves a normalization procedure (Humayun et al., 2010).

partial melting experiments of peridotite (Hirose and Kushiro, 1993; Walter, 1998) and model 1 and 10% partial melts of peridotite derived from multiple saturation experiments (Longhi, 2002) at 3 GPa (corrected to equilibrium with olivine with  $Mg\# = 0.898$ , Section 4.2.) in Fig. 6. Compared with the lowest melt fraction experiments from the direct melting experiments, the 0% melt has lower Al<sub>2</sub>O<sub>3</sub> resulting from the persistence of garnet in the residue. Low-degree melts estimated by Longhi (2002) are saturated in garnet, but are also richer in Al<sub>2</sub>O<sub>3</sub> than the low degree melts determined by MISE. The coexisting pyroxenes in the experiments of Longhi (2002) are also comparatively enriched in Al<sub>2</sub>O<sub>3</sub> (5–9 wt.% compared to 5–6 wt.% from the MISE data, Table 3). The CaO content of the 0% melt is similar to low melt fraction compositions from Hirose and Kushiro (1993) and Walter (1998), but significantly higher than the 1% melt of PUM predicted by Longhi (2002).

As expected, the incompatible elements TiO<sub>2</sub> and Na<sub>2</sub>O are more enriched in the 0% melt than in higher-degree melts (~15%) produced in previous experimental studies at 3 GPa (Hirose and Kushiro, 1993; Walter, 1998). The TiO<sub>2</sub> concentration is also greater than that estimated by Longhi (2002) for a near-solidus partial melt, suggesting

that Longhi's value of  $D_{Ti}$  was overestimated. As discussed in greater detail below, a precise determination of this TiO<sub>2</sub> partition coefficient is key to our understanding of the lithologic character of the OIB source region.

#### 4.2. Comparison with OIB

To evaluate the hypothesis that some alkalic OIB are derived from partial melting of volatile-poor peridotite requires compilation of a dataset of magmas that are potentially parental to observed OIB compositions and plausibly in equilibrium with peridotite near its solidus. We began by selecting glass or whole rock compositions from a wide range of OIB localities typified by alkalic lavas (see Fig. 6 caption for listing) from the GEOROC database (<http://georoc.mpch-mainz.gwdg.de/georoc/>, accessed 08/17/2009) with MgO contents  $\geq 10$  wt.% to minimize incorporation of lavas that experienced complex fractionation histories. We then corrected these compositions for olivine fractionation by adding or subtracting equilibrium olivine ( $K_D^{Fe-Mg} = 0.32$ , calculated from  $Mg^{2+}$  and  $Fe^{2+}$  in the melt, treating 10% of the iron in the melt as  $Fe^{3+}$ ) in 0.001% increments until the melts were in equilibrium with the olivine composition present in our experiments ( $Mg\# = 0.898$ ). We acknowledge that some lavas with  $\geq 10$  wt.% MgO may also have experienced cpx fractionation or accumulation. Below we consider briefly the potential influence of cpx addition or subtraction on similarities between OIB compositions and near-solidus partial melts of peridotite, but a rigorous evaluation of any such relation would be best suited to a focused regional study in which petrographic data could be integrated into a suitable fractionation correction.

The incipient partial melt of garnet lherzolite at 3 GPa has a strong resemblance to plausible parental compositions of many alkalic lavas from oceanic islands (Fig. 6). Concentrations of SiO<sub>2</sub>, CaO, Na<sub>2</sub>O, and TiO<sub>2</sub>, and to a lesser degree, MgO plot within the fields defined by the fractionation-corrected OIB. Of course, a single composition cannot span all of the range derived from OIB compositions, but it is apparent that very small degrees of partial melting of garnet peridotite produce alkalic magmas with similarities to those that could be parental to some intraplate oceanic basalts. However, there are key differences in major element compositions between the near-solidus melt of garnet peridotite at 3 GPa and liquids potentially parental to nearly all alkalic OIB and these differences suggest that most such lavas do not have such a simple origin. Most notably, the incipient partial melt has more Al<sub>2</sub>O<sub>3</sub> and less FeO\* and MgO than the field defined by fractionation-corrected OIB (Fig. 6). Also many of the possible parental magmas have more TiO<sub>2</sub> than the partial melt.

Enrichments in TiO<sub>2</sub> are a salient character of alkalic basalts from oceanic islands (Dasgupta et al., 2007a; Prytulak and Elliott, 2007), with concentrations exceeding 2 wt.% in most calculated parental liquids and 3 wt.% in many (Fig. 6). If these originate from normal peridotite, they must be derived from very small degrees of partial melting. The incipient partial melt documented here has  $2.5 \pm 0.2$  wt.% TiO<sub>2</sub>. Combining measured concentrations of TiO<sub>2</sub> in the melt and minerals (final iteration, Table 3) and the sub-solidus mineral mode (Table 1) gives a value of  $D_{Ti}^{gtherz/melt}$  equal to 0.069. Thus, primary partial melts with  $>2$  wt.% TiO<sub>2</sub> could be derived only from melt fractions  $<2\%$  for a source composition similar to KLB-1 and  $<4\%$  for a primitive mantle source with 0.2 wt.% TiO<sub>2</sub> (Table 1). Parental OIB with  $>3$  wt.% TiO<sub>2</sub> cannot be derived from primitive mantle at any melt fraction.

The genesis of parental OIB with  $>3$  wt.% TiO<sub>2</sub> requires a TiO<sub>2</sub>-enriched source, such as metasomatized peridotite or pyroxenite (Dasgupta et al., 2007a). Prytulak and Elliott (2007) made much the same point based on their estimates of peridotite/melt partitioning of TiO<sub>2</sub>, though it is apparent that Prytulak and Elliott (2007) applied too large a value of  $D_{Ti}^{gtherz/melt}$  (0.089), and this led them to exaggerate the range of OIB compositions that require exotic sources. However, a more accurate determination of  $D_{Ti}^{gtherz/melt}$  shows that even TiO<sub>2</sub>-

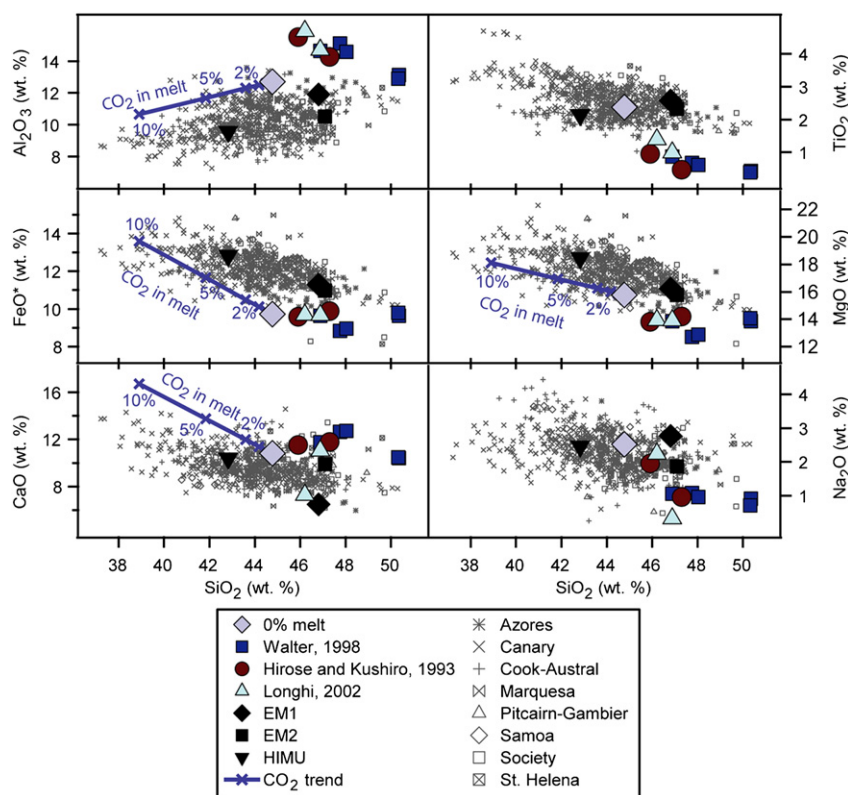


**Fig. 6.** Comparison of the 3 GPa 0% melt with OIB compositions. OIB compositions are from the GEOROC database (<http://georoc.mpch-mainz.gwdg.de/georoc/>, accessed 08/17/2009). The localities represented are the Azores, the Canary Islands, the Cook and Austral Islands, the Marquesas, Samoa, the Society Islands, and St. Helena (see Supplementary material for a complete list of references). Only basalts with  $>10\%$  MgO were selected to minimize inclusion of melt compositions that were significantly altered by cpx fractionation. Olivine was added or subtracted from the melt compositions in 0.001% increments until they were in equilibrium with Fo89.8 (see Section 4.2). Blue squares: partial melts of KR4003 peridotite at 3 GPa ( $F=14\text{--}53\%$ ; Walter, 1998). Red diamonds are partial melts of KLB-1 at 3 GPa ( $F=7\text{--}27\%$ ; Hirose and Kushiro, 1993). Blue triangles: model 1% (lower  $\text{SiO}_2$ ) and 10% partial melt compositions of fertile peridotite at 3 GPa (Longhi, 2002). Large black symbols are model values of primitive melts from the EM and HIMU sources (Jackson and Dasgupta, 2008). The effects of adding  $\text{CO}_2$  to the 0% melt at 3 GPa are shown for CaO,  $\text{SiO}_2$ , and  $\text{Al}_2\text{O}_3$ . Each of these compositions was also corrected by olivine addition/subtraction to equilibrium with Fo89.8 in order to allow for a more meaningful comparison with the corrected OIB compositions.  $\text{CO}_2$ -addition trends are from the 3 GPa carbonated peridotite experiments of Dasgupta et al. (2007a). To adjust for effects of temperature and melt fraction on these partial melts, temperature trends were determined for  $\text{SiO}_2$ ,  $\text{Al}_2\text{O}_3$ , MgO, and CaO from volatile-free peridotite partial melting experiments at 3 GPa (Walter, 1998). The slopes of these trends were used to correct the compositions of Dasgupta et al. (2007a), normalized on a volatile-free basis, to 1455 °C (KLB-1ox 3-GPa solidus).  $\text{FeO}^*$  in the Walter (1998) experiments does not appear to depend on temperature, so no temperature correction was applied. The temperature-corrected melt compositions were plotted against  $\text{CO}_2$ , and linear trends were determined and applied to our near-solidus melt composition.

enriched peridotite can generate high  $\text{TiO}_2$ -OIB only at relatively small degrees of partial melting. For example, in the database of 487 peridotite xenoliths compiled by Herzberg et al. (1988),  $<6\%$  have  $>0.2$  wt.% and  $<1\%$  have  $>0.3$  wt.%  $\text{TiO}_2$ . Generation of primary liquids with  $>3$  wt.%  $\text{TiO}_2$  from a source with 0.3 wt.%  $\text{TiO}_2$  requires melt fractions of 4% or smaller. The  $\text{TiO}_2$  enrichments in some OIB may be generated from higher melt fractions if their sources contain pyroxenites or have been metasomatized by partial melts of pyroxenites, which can be highly enriched in  $\text{TiO}_2$  (Dasgupta et al., 2006; Kogiso and Hirschmann, 2006; Pertermann and Hirschmann, 2003).

Compared to the incipient partial melt of peridotite at 3 GPa, the low  $\text{Al}_2\text{O}_3$ , high  $\text{FeO}^*$ , and high MgO in alkalic OIB could have three possible origins. One is that they originate in part owing to a  $\text{CO}_2$ -enriched garnet peridotite source and this is discussed in greater detail below. Other explanations include the possible role of enriched olivine-poor heterogeneities and the effects of pressures greater than 3 GPa. Note that cpx fractionation (or accumulation) would enhance (or diminish) both  $\text{FeO}^*$  and  $\text{Al}_2\text{O}_3$  concentrations of residual melts, and hence likely cannot explain the combined  $\text{FeO}^*$  enrichment and  $\text{Al}_2\text{O}_3$  depletion of parental OIB relative to small degree partial melts of garnet lherzolite.

The most straightforward explanation for high  $\text{FeO}^*$  in alkalic OIB is that it is owing to contributions from an Fe-enriched source (Humayun et al., 2004; Qin and Humayun, 2008), derived presumably

from refertilization by recycled crust, or from a distinct Fe-rich source in the deep mantle, perhaps from chemical interactions with the core (Humayun et al., 2004). A refertilized source is consistent with the constraints provided by  $\text{TiO}_2$ -enrichments, particularly for compositions with  $\text{TiO}_2 > 3$  wt.%. An Fe-enriched source would also account for the high apparent MgO contents of fractionation-corrected OIB, which have all been adjusted to be in equilibrium with olivine with forsterite content of 0.898. If in fact the liquids parental to alkalic OIB come from a more Fe-enriched source, then the assumed Mg# of the olivine in that source is likely too great, the compositions calculated in Fig. 6 are overcorrected for olivine fractionation, and the true parental liquids of alkalic OIB should have lower MgO than indicated. Finally, if Fe-enriched sources of OIB are pyroxenites, they also may account for low  $\text{Al}_2\text{O}_3$  concentrations (Kogiso and Hirschmann, 2006).

An alternative hypothesis that may account for low  $\text{Al}_2\text{O}_3$  and high MgO and  $\text{FeO}^*$  contents of alkalic OIB is formation from typical garnet peridotite at higher pressures (e.g., 4–5 GPa, Putirka, 2008; Walter, 1998), corresponding to initial melting at greater depths (125–155 km; Dasgupta et al., 2010). The enrichments in MgO and  $\text{FeO}^*$  would derive from the higher temperature of melting (Putirka, 2008), whereas lower  $\text{Al}_2\text{O}_3$  is imposed by expansion of the stability field of garnet. This presents an appealing explanation for the  $\text{FeO}^*$ -MgO- $\text{Al}_2\text{O}_3$  systematics of alkalic OIB, but we emphasize that the high  $\text{TiO}_2$  of such lavas requires melting at small degrees, and at least for the

case of nominally volatile-free mantle, we question whether this combination is geodynamically viable. Assuming that OIB derive from buoyant upwellings, we see no reason why such upwelling beneath oceanic lithosphere would be impeded at depths shallower than 125–155 km, as the lithosphere–asthenosphere boundary is <100 km thick even for mature oceanic lithosphere (Kumar and Kawakatsu, 2011). Continued upwelling and melting would produce high-degree partial melts at shallower (~100 km) depths (e.g., Ellam, 1992; Humphreys and Niu, 2009). Such melts would be tholeiitic (Walter, 1998) and low in TiO<sub>2</sub> and therefore unlike typical alkalic OIB. Deep initiation of partial melting may be appropriate for localities such as Hawaii (Lee et al., 2009), where tholeiitic partial melts are abundant, but evidence for such melts in the principal alkalic OIB localities (see caption to Fig. 6) is lacking. Deep initiation of partial melting owing to volatiles, with small associated increases in melt fraction with decompression (e.g., Asimow and Langmuir, 2003; Dasgupta et al., 2007b) could produce deep alkalic melts at small melt fraction, and this is worthy of further consideration. But for low Al<sub>2</sub>O<sub>3</sub> and high FeO\* alkalic OIB to be derived from small degree partial melting of nominally volatile-free peridotite at 125–155 km depths requires a mechanism that allows extraction of these melts while suppressing higher degree partial melts resulting from upwelling and melting between 125 and 155 km and the base of the lithosphere.

Deep initiation of partial melting near the solidus of nominally volatile-free peridotite requires high mantle potential temperatures. Intersection of the solidus at 4 and 5 GPa requires potential temperatures of 1500 and 1565 °C, respectively (Hirschmann, 2000). Such high potential temperatures are consistent with those inferred from many OIB localities, including those represented in Fig. 6, based on consideration of FeO\*–MgO–SiO<sub>2</sub> (Putirka, 2008). Similarly, Dasgupta et al. (2010) obtained comparable depths of equilibration for alkalic OIB based on SiO<sub>2</sub>–barometry of fractionation-corrected lavas. Putirka (2008) also used FeO\*–MgO–SiO<sub>2</sub> systematics to infer high melt fractions, averaging 12% for the alkalic OIB localities depicted in Fig. 6. However, such high melt fractions are not easily reconcilable with enrichments in TiO<sub>2</sub>. If the magmas come from normal peridotite, their TiO<sub>2</sub> enrichments require that they derive from small degrees of melting. Conversely, if they come from higher degree partial melts of enriched peridotites or pyroxenites, then the calculated temperatures and pressures are based on incorrect assumptions about composition of olivine in the source and therefore about the MgO contents of primary liquids. Thus, the temperatures and melt fractions inferred by Putirka (2008) for alkalic OIB (but not necessarily for tholeiitic OIB such as Hawaii or Iceland) are questionable and interpretations of potential temperatures for associated hot-spots should be considered with caution.

#### 4.3. Effects of small amounts of CO<sub>2</sub> in the melt phase

Differences in composition between parental alkalic OIB and near-solidus partial melt of garnet peridotite may also be related to modest concentrations of CO<sub>2</sub> in the source. Experiments by Dasgupta et al. (2007a) demonstrate that dissolved CO<sub>2</sub> has the effect of increasing FeO\* and MgO and diminishing Al<sub>2</sub>O<sub>3</sub> in partial melts, as well as increasing CaO and decreasing SiO<sub>2</sub>. This is illustrated in Fig. 6, which uses the trends in composition–CO<sub>2</sub> concentration from the experiments of Dasgupta et al. (2007a) to project the compositional effect of variable concentrations of dissolved CO<sub>2</sub> in the near-solidus partial melt.

The resulting vectors, while influencing all of the aforementioned oxides towards compositions increasingly similar to those of alkalic OIB, do not pass through the largest population of OIB compositions. This is because the most pronounced effect of dissolved CO<sub>2</sub> is to diminish SiO<sub>2</sub> concentrations. Therefore, magmas produced from partial melting of carbonated peridotite with high FeO\* and MgO and low Al<sub>2</sub>O<sub>3</sub>, similar to typical alkalic OIB primary liquids, would have

SiO<sub>2</sub> concentrations significantly lower than plausible parental liquids.

Some alkalic OIB, including those from the Canary Islands and, more generally, those with strong HIMU signatures, are characterized by particularly low SiO<sub>2</sub> and high CaO (Fig. 6). As illustrated in Fig. 6, at 3 GPa small-degrees of partial melting of a peridotite source with variable concentrations of CO<sub>2</sub> would produce an array of melt compositions that resemble the spectrum of low-SiO<sub>2</sub>, high-CaO/Al<sub>2</sub>O<sub>3</sub> melts from the Canary Islands. Similarly, the presence of 1–2 wt.% CO<sub>2</sub> in a small-degree partial melt (corresponding to a source concentration of 100–200 ppm for a 1% melt) drives its composition toward the major element characteristics of HIMU end-member basalts identified by Jackson and Dasgupta (2008; Fig. 6). Thus, the distinct compositional characteristics of HIMU-related OIB may be owing to a CO<sub>2</sub>-enriched source, though further experiments are required to determine the detailed effects of CO<sub>2</sub> on low-degree partial melts of peridotite. On the other hand, CO<sub>2</sub> enrichment alone cannot account for more typical compositions of OIB and in particular cannot account for those with strong EM signatures (Jackson and Dasgupta, 2008; Fig. 6), as these are comparatively enriched in SiO<sub>2</sub> and low in CaO. OIB with strong EM signatures therefore must have either metasomatically-enriched or non-peridotitic components in their sources.

Importantly, the CO<sub>2</sub>-addition vectors indicated in Fig. 6 are derived from an isobaric series of experiments where dissolved CO<sub>2</sub> concentrations vary inversely with melt fraction. The influence of variable amounts of CO<sub>2</sub> on near-solidus melts and the influence of CO<sub>2</sub> on varying extents of polybaric partial melting may not be the same. For example, the indicated diminished Al<sub>2</sub>O<sub>3</sub> may be related to increased stability of garnet with diminishing melt fraction, rather than the direct effects of dissolved CO<sub>2</sub>. On the other hand, the strong influence of dissolved CO<sub>2</sub> on SiO<sub>2</sub> of peridotite-saturated magmas is robust, as peridotite-saturated liquids show a nearly identical SiO<sub>2</sub>–CO<sub>2</sub> trend irrespective of melt fraction, melt composition, temperature, or pressure (Dasgupta et al., 2007a). A more detailed understanding of the influence of variable amounts of CO<sub>2</sub> on small-degree partial melts similar to OIB awaits study of the near solidus partial melting of peridotite in which melt fraction and CO<sub>2</sub> are independent variables.

#### 4.4. The potential role of K<sub>2</sub>O as a metasomatic agent in the OIB source region

The near-solidus partial melt determined in this study has ~1 wt.% K<sub>2</sub>O and derives from a peridotite with initial K<sub>2</sub>O = 0.003 ± 0.001 wt.% (see Appendix). These concentrations are less than those one might expect from incipient partial melting of the depleted MORB source (DMM), which has 0.006 wt.% K<sub>2</sub>O (Workman and Hart, 2005; Table 1). More enriched sources, such as those one might expect for OIB, would produce significantly more potassic near-solidus partial melts. For example, primitive mantle has 0.029 wt.% K<sub>2</sub>O (Table 1, McDonough and Sun, 1995) and similar enrichments are typical of xenoliths from the continental lithosphere (e.g., Menzies and Murthy, 1980). Also, EM sources, which may be influenced by recycled crustal components and most importantly, recycled sediments (Chauvel et al., 2008; Eiler et al., 1997; Eisele et al., 2002), could have marked K<sub>2</sub>O enrichments (Spandler et al., 2010). Consequently, investigation of the influence of K<sub>2</sub>O on near-solidus partial melting is of interest.

Differing concentrations of K<sub>2</sub>O in source peridotites are expected to alter solidus temperatures (Hirschmann, 2000), and concomitant changes in the K<sub>2</sub>O contents of near-solidus melts may have other effects on the major element chemistry of those melts. Hirschmann (2000) demonstrated that the solidi of different peridotites used in experimental studies at 3 GPa decreased with increasing total alkali content. The solidus of KLB-10x determined by our near-solidus experiments (K<sub>2</sub>O = 0.014 ± 0.002 wt.%, 1445 °C) and the temperature at which the last three MISE iterations produced nearly the ideal

20% experimental melt fraction (model peridotite  $K_2O = 0.003 \pm 0.001$  wt.%, 1455 °C) may be related to differences in the  $K_2O$  content of their sources. Additional  $K_2O$  is also expected to increase  $SiO_2$  in the melt (Hirschmann et al., 1998), which could have the effect of driving peridotite partial melts toward compositions of EM-flavored lavas (Jackson and Dasgupta, 2008). Further experiments on the effects of increased  $K_2O$  in the peridotite will be explored in a future work.

## 5. Conclusions

The MISE method provides a robust technique for determining the composition of near-solidus partial melts of mantle lithologies. Identification of the incipient partial melt of garnet peridotite at 3 GPa provides a key constraint on the genesis of oceanic island basalts. Near-solidus partial melts of typical upper mantle garnet peridotite have similarities to many OIB and may be a significant component of these important lavas, but they cannot be the sole source of typical alkalic OIB. Basalts derived from key mantle source regions (HIMU, EM1, EM2) or their hybrids must have a complex origin that includes contributions from partial melts of peridotite that have been altered by  $CO_2$  (Dasgupta et al., 2007a), other metasomatic enrichments (Humayun et al., 2004; Pilet et al., 2005), or by partial melting of pyroxenite (Hirschmann et al., 2003).

Supplementary materials related to this article can be found online at doi:10.1016/j.epsl.2011.06.008

## Acknowledgments

We thank Ellery Frahm for his assistance and his superior efforts maintaining an excellent electron microprobe facility at the University of Minnesota. This paper benefited from constructive reviews from Mike Walter and Claude Herzberg. This work was supported by NSF grants EAR0609967 and EAR1019744 to M.M.H.

## References

- Asimow, P.D., Langmuir, C.H., 2003. The importance of water to oceanic mantle melting regimes. *Nature* 421, 815–820.
- Baker, M.B., Hirschmann, M.M., Ghiorso, M.S., Stolper, E.M., 1995. Compositions of near-solidus peridotite melts from experiments and thermodynamic calculations. *Nature* 375, 308–311.
- Baker, J.A., Menzies, M.A., Thirlwall, M.F., Macpherson, C.G., 1997. Petrogenesis of quaternary intraplate volcanism, Sana'a, Yemen: implications for plume–lithosphere interaction and polybaric melt hybridization. *J. Petrol.* 38, 1359–1390.
- Chauvel, C., Lewin, E., Carpentier, M., Arndt, N.T., Marini, J.C., 2008. Role of recycled oceanic basalt and sediment in generating the HF–Nd mantle array. *Nat. Geosci.* 1, 64–67.
- Class, C., Altherr, R., Volker, F., Eberz, G., McCulloch, M.T., 1994. Geochemistry of Pliocene to quaternary alkali basalts from the Huri Hills, northern Kenya. *Chem. Geol.* 113, 1–22.
- Cook, C., Briggs, R.M., Smith, I.E.M., Maas, R., 2005. Petrology and geochemistry of intraplate basalts in the South Auckland Volcanic Field, New Zealand: evidence for two coeval magma suites from distinct sources. *J. Petrol.* 46, 473–503.
- Dasgupta, R., Hirschmann, M.M., Stalker, K., 2006. Immiscible transition from carbonate-rich to silicate-rich melts in the 3 GPa melting interval of eclogite plus  $CO_2$  and genesis of silica-undersaturated oceanic island lavas. *J. Petrol.* 47, 647–671.
- Dasgupta, R., Hirschmann, M.M., Smith, N.D., 2007a. Partial melting experiments of peridotite  $CO_2$  at 3 GPa and genesis of alkalic ocean island basalts. *J. Petrol.* 48, 2093–2124.
- Dasgupta, R., Hirschmann, M.M., Smith, N.D., 2007b. Water follows carbon:  $CO_2$  incites deep silicate melting and dehydration beneath mid-ocean ridges. *Geology* 35, 135–138.
- Dasgupta, R., Jackson, M.G., Lee, C.T.A., 2010. Major element chemistry of ocean island basalts – conditions of mantle melting and heterogeneity of mantle source. *Earth Planet. Sci. Lett.* 289, 377–392.
- Davis, F.A., Tangeman, J.A., Tenner, T.J., Hirschmann, M.M., 2009. The composition of KLB-1 peridotite. *Am. Mineral.* 94, 176–180.
- Eiler, J.M., Farley, K.A., Valley, J.W., Hauri, E., Craig, H., Hart, S.R., Stolper, E.M., 1997. Oxygen isotope variations in ocean island basalt phenocrysts. *Geochem. Cosmochim. Acta* 61, 2281–2293.
- Eisele, J., Sharma, M., Galer, S.J.G., Blichert-Toft, J., Devey, C.W., Hofmann, A.W., 2002. The role of sediment recycling in EM-1 inferred from Os, Pb, Hf, Nd, Sr isotope and trace element systematics of the Pitcairn hotspot. *Earth Planet. Sci. Lett.* 196, 197–212.
- Ellam, R.M., 1992. Lithospheric thickness as a control on basalt geochemistry. *Geology* 20, 153–156.
- Herzberg, C., 2006. Petrology and thermal structure of the Hawaiian plume from Mauna Kea volcano. *Nature* 444, 605–609.
- Herzberg, C., Feigenson, M., Skuba, C., Ohtani, E., 1988. Majorite fractionation recorded in the geochemistry of peridotites from South-Africa. *Nature* 332, 823–826.
- Herzberg, C., Gasparik, T., Sawamoto, H., 1990. Origin of mantle peridotite – constraints from melting experiments to 16.5 GPa. *J. Geophys. Res.-Solid Earth Planets* 95, 15779–15803.
- Herzberg, C., Asimow, P.D., Arndt, N., Niu, Y.L., Leshar, C.M., Fitton, J.G., Cheadle, M.J., Saunders, A.D., 2007. Temperatures in ambient mantle and plumes: constraints from basalts, picrites, and komatiites. *Geochem. Geophys. Geosyst.* 8, Q02006.
- Hirose, K., Kushiro, I., 1993. Partial melting of dry peridotites at high-pressures – determination of compositions of melts segregated from peridotite using aggregates of diamond. *Earth Planet. Sci. Lett.* 114, 477–489.
- Hirschmann, M.M., 2000. Mantle solidus: experimental constraints and the effects of peridotite composition. *Geochem. Geophys. Geosyst.* 1, 2000GC000070.
- Hirschmann, M.M., Dasgupta, R., 2007. A modified iterative sandwich method for determination of near-solidus partial melt compositions I. Theoretical considerations. *Contrib. Mineral. Petrol.* 154, 635–645.
- Hirschmann, M.M., Baker, M.B., Stolper, E.M., 1998. The effect of alkalis on the silica content of mantle-derived melts. *Geochem. Cosmochim. Acta* 62, 883–902.
- Hirschmann, M.M., Kogiso, T., Baker, M.B., Stolper, E.M., 2003. Alkalic magmas generated by partial melting of garnet pyroxenite. *Geology* 31, 481–484.
- Hofmann, A.W., 1997. Mantle geochemistry: the message from oceanic volcanism. *Nature* 385, 219–229.
- Humayun, M., Qin, L.P., Norman, M.D., 2004. Geochemical evidence for excess iron in the mantle beneath Hawaii. *Science* 306, 91–94.
- Humayun, M., Davis, F.A., Hirschmann, M.M., 2010. Major element analysis of natural silicates by laser ablation ICP-MS. *J. Anal. At. Spectrom.* 25, 998–1005.
- Humphreys, E.R., Niu, Y., 2009. On the composition of ocean island basalts (OIB): the effects of lithospheric thickness variation and mantle metasomatism. *Lithos* 112, 118–136.
- Jackson, M.G., Dasgupta, R., 2008. Compositions of HIMU, EM1, and EM2 from global trends between radiogenic isotopes and major elements in ocean island basalts. *Earth Planet. Sci. Lett.* 276, 175–186.
- Kogiso, T., Hirschmann, M.M., 2006. Partial melting experiments of bimineraleclogite and the role of recycled mafic oceanic crust in the genesis of ocean island basalts. *Earth Planet. Sci. Lett.* 249, 188–199.
- Kogiso, T., Hirose, K., Takahashi, E., 1998. Melting experiments on homogeneous mixtures of peridotite and basalt: application to the genesis of ocean island basalts. *Earth Planet. Sci. Lett.* 162, 45–61.
- Kogiso, T., Hirschmann, M.M., Frost, D.J., 2003. High-pressure partial melting of garnet pyroxenite: possible mafic lithologies in the source of ocean island basalts. *Earth Planet. Sci. Lett.* 216, 603–617.
- Kumar, P., Kawakatsu, H., 2011. Imaging the seismic lithosphere–asthenosphere boundary of the oceanic plate. *Geochem. Geophys. Geosyst.* 12, Q01006.
- Lee, C.T.A., Luffi, P., Plank, T., Dalton, H., Leeman, W.P., 2009. Constraints on the depths and temperatures of basaltic magma generation on Earth and other terrestrial planets using new thermobarometers for mafic magmas. *Earth Planet. Sci. Lett.* 279, 20–33.
- Longhi, J., 2002. Some phase equilibrium systematics of lherzolite melting: I. *Geochem. Geophys. Geosyst.* 3, 1020.
- McDonough, W.F., Sun, S.S., 1995. The composition of the earth. *Chem. Geol.* 120, 223–253.
- McKenzie, D., O'Nions, R.K., 1995. The source regions of ocean island basalts. *J. Petrol.* 36, 133–159.
- Menzies, M., Murthy, V.R., 1980. Enriched mantle – Nd and Sr isotopes in diopsides from kimberlite nodules. *Nature* 283, 634–636.
- Mysen, B.O., Kushiro, I., 1977. Compositional variations of coexisting phases with degree of melting of peridotite in the upper mantle. *Am. Mineral.* 62, 843–865.
- Pertermann, M., Hirschmann, M.M., 2003. Anhydrous partial melting experiments on MORB-like eclogite: phase relations, phase compositions and mineral–melt partitioning of major elements at 2–3 GPa. *J. Petrol.* 44, 2173–2201.
- Pickering-Witter, J., Johnston, A.D., 2000. The effects of variable bulk composition on the melting systematics of fertile peridotitic assemblages. *Contrib. Mineral. Petrol.* 140, 190–211.
- Pilet, S., Hernandez, J., Sylvester, P., Poujol, M., 2005. The metasomatic alternative for ocean island basalt chemical heterogeneity. *Earth Planet. Sci. Lett.* 236, 148–166.
- Prytulak, J., Elliott, T., 2007.  $TiO_2$  enrichment in ocean island basalts. *Earth Planet. Sci. Lett.* 263, 388–403.
- Putirka, K., 2008. Excess temperatures at ocean islands: implications for mantle layering and convection. *Geology* 36, 283–286.
- Qin, L.P., Humayun, M., 2008. The Fe/Mn ratio in MORB and OIB determined by ICP-MS. *Geochem. Cosmochim. Acta* 72, 1660–1677.
- Robinson, J.A.C., Wood, B.J., Blundy, J.D., 1998. The beginning of melting of fertile and depleted peridotite at 1.5 GPa. *Earth Planet. Sci. Lett.* 155, 97–111.
- Salters, V.J.M., Stracke, A., 2004. Composition of the depleted mantle. *Geochem. Geophys. Geosyst.* 5, Q05004.
- Schwarzer, R.R., Rogers, J.J.W., 1974. A worldwide comparison of alkali olivine basalts and their differentiation trends. *Earth Planet. Sci. Lett.* 23, 286–296.
- Spandler, C., Yaxley, G., Green, D.H., Scott, D., 2010. Experimental phase and melting relations of metapelite in the upper mantle: implications for the petrogenesis of intraplate magmas. *Contrib. Mineral. Petrol.* 160, 569–589.
- Takahashi, E., 1986. Melting of a dry peridotite KLB-1 up to 14 GPa – implications on the origin of peridotitic upper mantle. *J. Geophys. Res.-Solid Earth Planets* 91, 9367–9382.

- Thomas, L.E., Hawkesworth, C.J., Van Calsteren, P., Turner, S.P., Rogers, N.W., 1999. Melt generation beneath ocean islands: a U–Th–Ra isotope study from Lanzarote in the Canary Islands. *Geochem. Cosmochim. Acta* 63, 4081–4099.
- Toplis, M.J., 2005. The thermodynamics of iron and magnesium partitioning between olivine and liquid: criteria for assessing and predicting equilibrium in natural and experimental systems. *Contrib. Mineral. Petrol.* 149, 22–39.
- Walter, M.J., 1998. Melting of garnet peridotite and the origin of komatiite and depleted lithosphere. *J. Petrol.* 39, 29–60.
- Wasylenki, L.E., Baker, M.B., Kent, A.J.R., Stolper, E.M., 2003. Near-solidus melting of the shallow upper mantle: partial melting experiments on depleted peridotite. *J. Petrol.* 44, 1163–1191.
- Workman, R.K., Hart, S.R., 2005. Major and trace element composition of the depleted MORB mantle (DMM). *Earth Planet. Sci. Lett.* 231, 53–72.
- Xirouchakis, D., Hirschmann, M.M., Simpson, J.A., 2001. The effect of titanium on the silica content and on mineral-liquid partitioning of mantle-equilibrated melts. *Geochem. Cosmochim. Acta* 65, 2201–2217.
- Yang, H.J., Frey, F.A., Clague, D.A., 2003. Constraints on the source components of lavas forming the Hawaiian North Arch and Honolulu volcanics. *J. Petrol.* 44, 603–627.
- Zindler, A., Hart, S., 1986. Chemical geodynamics. *Annu. Rev. Earth Planet. Sci.* 14, 493–571.